| | |
|---|---|
| **Preprint Title** | Optoelectronic Properties of Polycyclic Aromatic Hydrocarbons of Various Sizes and Shapes: A DFT Study |
| **Authors** | Ramachandran Rakhi and Cherumuttathu H. Suresh |
| **Publication Date** | 13 Okt. 2020 |
| **Article Type** | Full Research Paper |
| **Supporting Information File 1** | Supporting Information.docx; 14.4 MB |
| **ORCID® iDs** | Cherumuttathu H. Suresh - https://orcid.org/0000-0001-7237-6638 |

# Optoelectronic Properties of Polycyclic Aromatic Hydrocarbons of Various Sizes and Shapes: A DFT Study

Ramachandran Rakhi[1,2], and Cherumuttathu H. Suresh[1,2]

[1]Chemical Sciences and Technology Division, CSIR–National Institute for Interdisciplinary Science and Technology (CSIR–NIIST), Thiruvananthapuram 695019, India.

[2]Academy of Scientific and Innovative Research (AcSIR), Ghaziabad 201002, India

*Correspondence to: Cherumuttathu H. Suresh (E-mail: sureshch@niist.res.in)*

## Abstract

Polycyclic aromatic hydrocarbons (PAHs) can be considered as graphene nanoflakes in which the edges are hydrogenated. Zigzag and armchair-edged PAHs possessing circular, parallelogram, rectangular and triangular shapes have been studied using M06L/6-31+G(d) level of density functional theory (DFT). Molecular electrostatic potential (MESP) analysis of the PAHs is done to characterize their electron distribution while the time-dependent DFT (TD-DFT) analysis was used for the absorption spectral analysis. MESP analysis clearly showed Clar's sextet like electronic arrangement in armchair-edged systems whereas zigzag-edged ones showed significant electron localization towards the edges. TD-DFT analysis casts light upon the absorption features of these systems, which followed a linear trends in absorption maximum ($\lambda_{max}$) for most of the armchair-edged systems with respect to the number of π-electrons. MESP analysis on the electron rich and electron deficient features of PAH systems led to the design of donor-spacer-acceptor type PAH-π-PAH systems (D-π-A systems)

wherein a conjugated diene moiety functions as the π-spacer. Though these systems behaved weakly as D-π-A systems, with the introduction of electron donating functional group $NMe_2$ on one PAH and electron withdrawing group COOH on the other led to the formation of strong D-π-A systems. The MESP features, frontier molecular orbital (FMO) distribution, and absorption spectral features supported their strong D-π-A character. Among the different shapes studied, the rectangular PAH moiety showed the most efficient tuning of HOMO-LUMO gap. The optical and electronic data of PAH, PAH-π-PAH and functionalized PAH-π-PAH systems shed light upon possible tuning of their optoelectronic properties for practical applications.

# Introduction

The field of molecular materials flourished in the 21st century after the isolation of graphene by Nobel Prize winners Geim and Novoselov,[1] even though the pioneering theoretical work was done by P. Wallace in the year 1947.[2] By definition, graphene is a polycyclic aromatic hydrocarbon (PAH) which is a flat monolayer of $sp^2$ carbon atoms packed into a two dimensional π-conjugated system,[3-5] having exceptional electronic, thermal and mechanical properties.[1,6] Despite being one atom thick, graphene can be optically visualized.[7,8] Together with this visibility, other remarkable optical properties like hot luminescence, saturable absorption, and broadband applicability renders graphene an ideal photonic and optoelectronic material.[9-17]

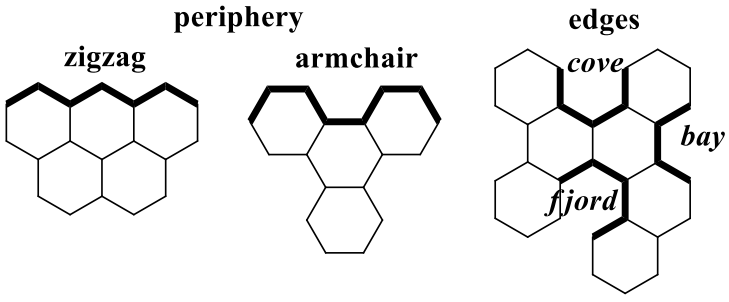


**Figure 1**. Different types of periphery and edges in PAHs.

Large flakes of graphene in which every ring are different from the other are termed nanographene,[3,18-23] the properties of which are largely influenced by the size and edge shape.[24-28] As the size of the PAH increases, the number of isomers possible also increases.[29] Graphene nanoflakes are stable than carbon nanotubes of similar size, but less stable than the corresponding fullerenes. In addition, large flakes have almost zero bandgap whereas small ones are semiconductors or insulators. Graphene nanoflakes tend to show new and unexpected electronic, optical, vibrational and magnetic properties based on the size and geometry. [24,25,30-35] For example, triphenylene and tetracene are made of four aromatic rings, the absorption maximum of former is at 265 nm and the same for latter is 471 nm, a much higher value. In addition, triphenylene is quite stable against oxidation whereas tetracene is easily oxidized. On the basis of resonance structures of PAH, Clar proposed the sextet rule which predicts the largest number of disjoint benzene-like $\pi$-conjugated moieties one can draw for a PAH. According to Clar's rule, triphenylene having three sextet rings is more aromatic and more stable than the isomer tetracene having only one sextet.[36-39] Two types of periphery (zigzag and armchair) and three types of edges (the bay, the cove and the fjord) are observed for PAHs, (Figure 1).[24] PAHs with armchair periphery are more resonance stabilized compared to those with the zigzag periphery, making zigzag ones more reactive so that larger PAHs with zigzag periphery is instantaneously converted to quinine in the air.[24 31] It is already proven that the HOMO-LUMO band gap engineering can be done by changing the size and the shape of graphene nanoflakes.[40] Large PAHs are present naturally, but graphene nanoflakes are very difficult to synthesize and are not found naturally.[41] Syntheses of nanoflakes are done,[42-45] but the growth and nucleation trends are yet to be understood. Both top-down[46-50] and bottom-up[43,51] approaches are adopted for synthesis. Extensive theoretical research on graphene nanoflakes have been done by various groups.[52-57]

Here we consider PAH molecules of various sizes and shapes as potential candidates for the design of donor or acceptor part of a donor-(π)spacer-acceptor (D-π-A) system. MESP analysis is used to evaluate the electron rich/deficient feature of a particular shape or size of the PAH. The electron rich PAH will be proposed suitable for the design of donor while a relatively electron deficient PAH will be suggested for the design of acceptor. Further, functionalization of the donor PAH is considered with $NMe_2$ substituent while an acceptor moiety COOH is proposed to improve the accepting ability of the acceptor PAH.

# Computational Methods

All the molecules are optimized using Gaussian16 suite of programs,[58] using the DFT method M06L/6-31+G(d).[59] The optimized geometries are confirmed as energy minima by vibrational frequency analysis. The electron density generated using M06L/6-31+G(d) method is used for molecular electrostatic potential (MESP) calculations. Using time-dependent density functional theory (TD-DFT)[60-63] technique at the same level of theory, the absorption and molecular orbital features of every set of molecules are derived.

# Results and Discussion

## PAH systems: structure

The PAHs are categorized into six groups on the basis of the overall shape of the molecule and the shape of their zigzag and armchair edges. A circular and parallelogram-shaped PAH can have armchair and zigzag edges. Armchair edged triangular-shaped PAH is also considered whereas a zigzag edged triangular shape is

not included in the study due to the requirement of odd number of C-H bonds to complete the shape (odd electron system). The sixth category belongs to rectangular-shaped PAHs. For such a shape, one side has to be zigzag edged while the adjacent side has to be armchair edged. In every set of molecules, 4 systems are analyzed in the present study, which are designated as $X_yN$, *where X = C, T, P* or *R* denoting circular, triangular, parallelogram and rectangular shaped structures respectively and y = *z, a* or *h* standing for zigzag, armchair and hybrid morphology, respectively. The notation *N* is used as a serial number (*1-4*) for the smallest to the largest system studied in each category. A representative set of molecules from each category is given in Figure 2.

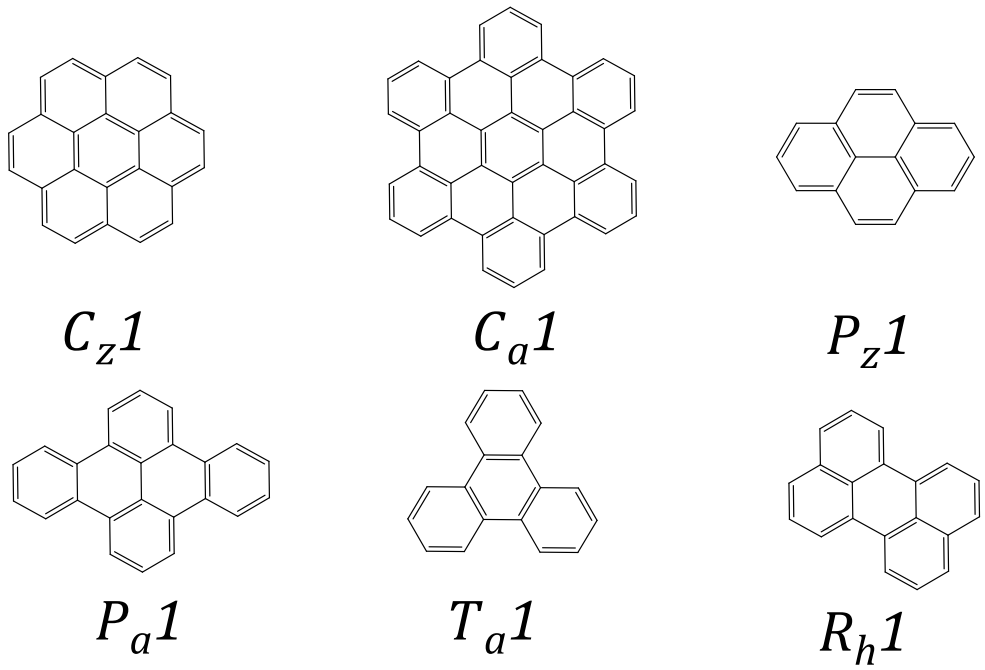


**Figure 2**. Representative set of PAH molecules under study

For the PAH systems, the number of π-electrons and number of π-electrons per CC bonds ($n_\pi$) are given in Table 1. The $n_\pi$ can be used as a simple measure to assess the π-electron density in every molecule. In every category, $n_\pi$ decreases as the size of the system increases because the number of CC bonds monotonically increases. The $C_xN$ systems show the lowest $n_\pi$ value.

**Table 1**. The number of π- electrons and ratio of the number of π electrons to the total number of CC bonds ($n_\pi$) in PAH systems.

| System | No. of π-ē | $n_\pi$ | System | No. of π-ē | $n_\pi$ | System | No. of π-ē | $n_\pi$ |
|---|---|---|---|---|---|---|---|---|
| | | 0.800 | | | 0.842 | | | 0.857 |
| *$C_z1$* | 24 | | *$P_z1$* | 16 | | *$T_a1$* | 18 | |
| | | 0.750 | | | 0.789 | | | 0.800 |
| *$C_z2$* | 54 | | *$P_z2$* | 30 | | *$T_a2$* | 36 | |
| | | 0.727 | | | 0.769 | | | 0.769 |
| *$C_z3$* | 96 | | *$P_z3$* | 48 | | *$T_a3$* | 60 | |
| | | 0.714 | | | 0.745 | | | 0.750 |
| *$C_z4$* | 150 | | *$P_z4$* | 70 | | *$T_a4$* | 90 | |
| | | 0.778 | | | 0.825 | | | 0.833 |
| *$C_a1$* | 42 | | *$P_a1$* | 24 | | *$R_h1$* | 20 | |
| | | 0.750 | | | 0.778 | | | 0.778 |
| *$C_a2$* | 72 | | *$P_a2$* | 54 | | *$R_h2$* | 42 | |
| | | 0.733 | | | 0.741 | | | 0.778 |
| *$C_a3$* | 132 | | *$P_a3$* | 96 | | *$R_h3$* | 74 | |
| | | 0.714 | | | 0.738 | | | 0.733 |
| *$C_a4$* | 184 | | *$P_a4$* | 152 | | *$R_h4$* | 110 | |

## PAH systems: MESP analysis

To understand the electronic characteristics of every PAH systems, the most negative valued MESP ($V_{min}$) in the molecules is determined.[64,65] MESP has been successfully demonstrated as an effective tool in studying PAH and other related systems,

especially to interpret Clar's aromatic sextet theory.[36-38] Figure 3 shows MESP features of a representative set of systems (the smallest member in every category). See supporting information for MESP isosurface for all the systems. The black dot in the MESP isosurface denotes the deepest $V_{min}$ and their values are given in Table 2 (cf. Figure S1 for MESP isosurface plots). A gradual decrease in the absolute value of the $V_{min}$ is observed with increase in the size of the PAH which indicates the diminishing electron richness due to the enhancement of electron delocalization.

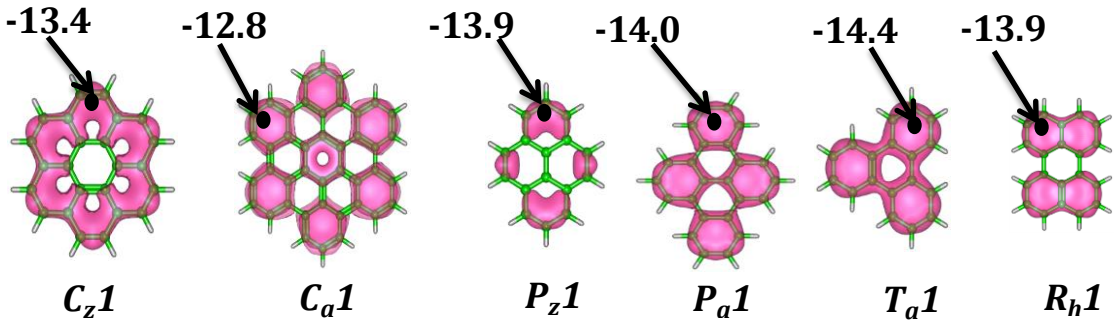


**Figure 3.** MESP features on smallest PAH system in all categories.

**Table 2.** $V_{min}$ values of all the PAH systems in kcal/mol.

| | $C_zN$ | $C_aN$ | $P_zN$ | $P_aN$ | $T_aN$ | $R_hN$ |
|---|---|---|---|---|---|---|
| *N=1* | -13.4 | -12.8 | -13.9 | -14.0 | -14.4 | -13.9 |
| *N=2* | -12.5 | -11.9 | -13.1 | -13.0 | -13.5 | -13.4 |
| *N=3* | -11.8 | -11.7 | -12.4 | -12.3 | -12.9 | -13.0 |
| *N=4* | -11.0 | -11.3 | -11.9 | -12.1 | -12.6 | -12.7 |

Plots showing the correlation between $n_\pi$ values and the corresponding $V_{min}$ values are given in Figure 4. The good linear relationships indicate that in a specific series, the π-electronic features gradually decrease with increase in the size of the molecule. The circular shaped systems (red dots in Figure 4) show the highest rate of decrease in π-electron density while the rectangular $R_hN$ systems (green dots) display the lowest.

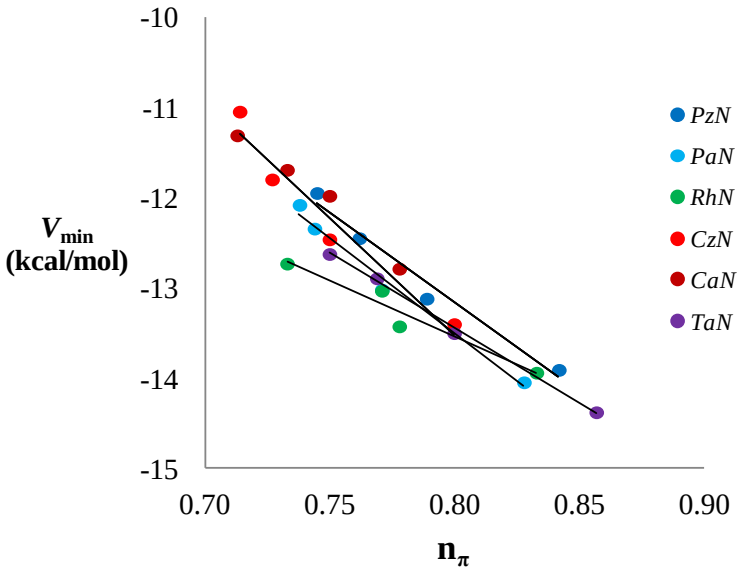


**Figure 4.** Graphs plotting $n_\pi$ values and $V_{min}$ values on all the PAH systems.

For $C_zN$, the electron localization can be observed in the peripheral rings in all the structures as evident from the $V_{min}$ values at the outermost rings. In the case of $C_aN$ systems, outermost aromatic rings with three C-H bonds show the most negative $V_{min}$. In $C_aN$ systems, the Clar's aromatic sextet retention are easily visualised, while for the $C_zN$ ones, Clar's sextet features of hexagons cannot be distinguished. In $C_zN$, the electron cloud as seen in MESP is localised strongly towards the outermost rings. This trend indicates that the armchair edged ones are more stabilised by aromaticity than the zigzag edged ones. The peripheral localization of the electron cloud is clearly visible in the MESP picture for $P_zN$ systems, whereas for the $P_aN$ ones, MESP features are clearly expressed as Clar's sextets. For $P_zN$ systems, the terminal rings with three C-H bonds show the most negative MESP features and for $P_aN$ type PAHs, the $V_{min}$ values are observed at the terminal rings with four C-H bonds. The peculiarity of armchair edged systems, as mentioned for $C_aN$ and $P_aN$ type PAHs are retained in the $T_aN$ systems also. The visualisation of Clar's sextet is evident by comparing with the Clar's structure for all $T_aN$. In this case, the $V_{min}$ values are observed at the corner rings of every structure, the magnitude of which gradually diminishes as the size increases.

The $V_{min}$ of $R_hN$ PAHs is observed at the corner rings in every system. For these systems, the constituting individual acene parts *viz.* naphthalene, anthracene, tetracene and pentacene can be visualised from the topology of MESP. A representative set of MESP features on armchair edged systems and their corresponding Clar's structures are given in Figure 5, to show the Clar's sextet like MESP localisation in these systems. In fact, *C*a2 is not a complete armchair edged system as it contains short zigzag portions too. Similarly, *C*a3 contains cove region while *C*a4 contains short zigzag portions and cove regions (supporting information). The sextet localization of electrons in the rings is the lowest for such mixed systems.

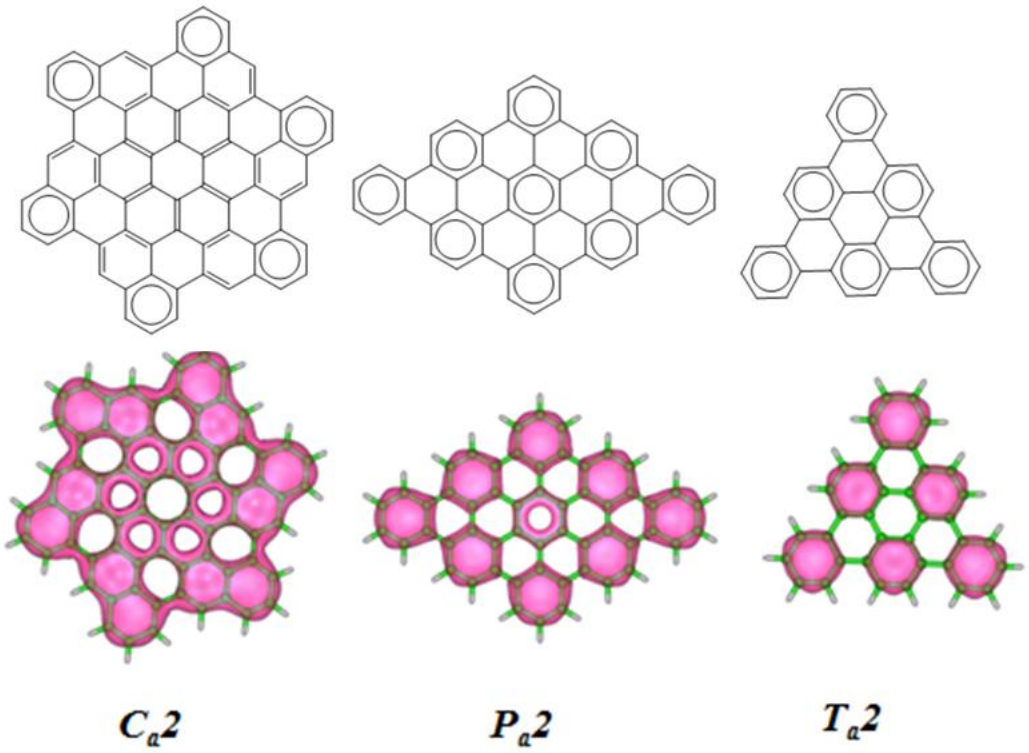


**Figure 5.** Figures of MESP isosurface of representative armchair edged PAHs with the corresponding Clar's structures.

## PAH-π-PAH systems: structure

Only the first member from each category of molecules ($C_z1$, $C_a1$, $P_z1$, $P_a1$, $T_a1$ and $R_h1$) is selected to design the PAH-π-spacer-PAH systems (PAH-π-PAH). The

selected π-spacer is *t*-butadiene moiety. These systems thus designed are named as *$C_z$1-$C_a$1, $C_z$1-$P_z$1, $P_a$1-$C_z$1, $T_a$1-$C_z$1, $C_z$1-$R_h$1, $P_z$1-$C_a$1, $P_a$1-$C_a$1, $T_a$1-$C_a$1, $R_h$1-$C_a$1, $P_a$1-$P_z$1, $T_a$1-$P_z$1, $P_z$1-$R_h$1, $T_a$1-$P_a$1, $P_a$1-$R_h$1, and $T_a$1-$R_h$1*. Naming is done in such a manner that the PAH system having the highest negative $V_{min}$ value is given first, followed by the name of the second PAH moiety. The most electron rich carbon of the PAH systems as seen in MESP topography (the carbon that appears nearest to the $V_{min}$ point) are selected to join the spacer butadiene moiety. Most of the designed systems possess perfect planar structures and the exceptions are *$R_h$1-$C_a$1, $C_z$1-$C_a$1, $C_z$1-$P_z$1, $P_a$1-$C_z$1, $T_a$1-$C_z$1,* and *$C_z$1-$R_h$1*. All the *$C_z$1* connected systems are non-planar. The slight amount of non-planarity observed is measured in terms of the largest twist angle between the conjugated diene and the PAH moieties. A representative set of one non-planar system *$C_z$1-$P_z$1* and a planar one *$T_a$1-$P_a$1* are shown in Figure 6. The dihedral angles made by both PAH parts with the diene are marked in the figure. In *$C_z$1-$P_z$1*, a dihedral angle 32° is visible between the *$C_z$1* end whereas the *$P_z$1* end is planar.

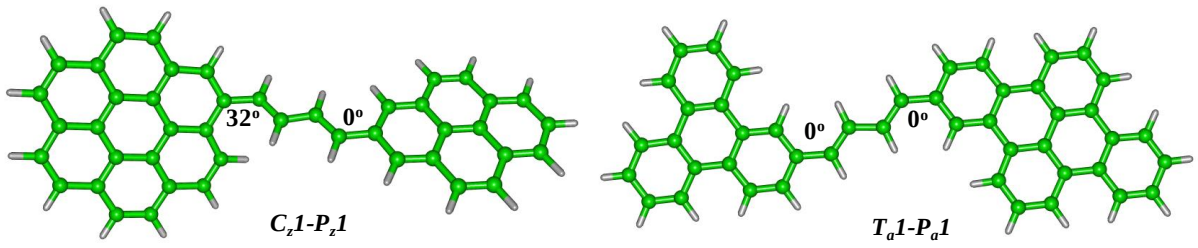


**Figure 6.** Optimised geometry of non-planar (*$C_z$1-$P_z$1*) and planar (*$T_a$1-$P_a$1*) systems (dihedral angle is marked in both the structures).

## PAH-π-PAH systems: MESP analysis

These systems are analyzed for their electronic features using the tool of MESP and the $V_{min}$ values on different parts of the systems are given in Table 3. The notations in Table 3 are color coded; the PAH moiety showing more electron rich character than

**Table 3.** $V_{min}$ values on different parts of PAH-π-PAH systems.

| System | $V_{min}$D (kcal/mol) | $V_{min}$S (kcal/mol) | $V_{min}$A (kcal/mol) |
|---|---|---|---|
| *$C_z1$-$C_a1$* | -12.8 | -13.6 | -12.4 |
| *$C_z1$-$P_z1$* | -13.4 | -14.3 | -13.3 |
| *$P_a1$-$C_z1$* | -13.5 | -13.9 | -13.0 |
| *$T_a1$-$C_z1$* | -13.7 | -14.0 | -13.2 |
| *$C_z1$-$R_h1$* | -13.3 | -13.8 | -13.0 |
| *$P_z1$-$C_a1$* | -13.0 | -13.6 | -12.6 |
| *$P_a1$-$C_a1$* | -13.4 | -13.3 | -12.5 |
| *$T_a1$-$C_a1$* | -13.5 | -13.6 | -12.4 |
| *$R_h1$-$C_a1$* | -13.2 | -13.8 | -12.5 |
| *$P_a1$-$P_z1$* | -13.7 | -14.0 | -13.2 |
| *$T_a1$-$P_z1$* | -13.8 | -14.3 | -13.2 |
| *$P_z1$-$R_h1$* | -13.6 | -14.7 | -13.4 |
| *$T_a1$-$P_a1$* | -13.7 | -13.7 | -13.6 |
| *$P_a1$-$R_h1$* | -13.5 | -13.8 | -13.2 |
| *$T_a1$-$R_h1$* | -13.7 | -13.9 | -13.4 |

the other is given in red color (donor moiety) while the other (acceptor moiety) is shown in blue color. $V_{min}$D represents the $V_{min}$ of donor moiety whereas $V_{min}$A represents the same for the acceptor moiety and $V_{min}$S is for the $V_{min}$ value of spacer unit (butadiene moiety). The connected PAH moieties have different values of MESP minima independent of the shape of these systems. The $V_{min}$ observed for a PAH portion in PAH-π-PAH is less negative than the full PAH. For example, consider *$T_a1$-$C_a1$* system, in which *$T_a1$* part has a $V_{min}$ of -13.5 kcal/mol, while the free *$T_a1$* system has a $V_{min}$

value -14.4 kcal/mol. Similarly, the PAH system $C_a1$ has $V_{min}$ value -12.8 kcal/mol, which is changed to a less negative value -12.4 kcal/mol in $T_a1$-$C_a1$ system. See supporting Information for MESP isosurface for all the systems. The spacer part is having the highest $V_{min}$ ranging from -13.3 to -14.7 kcal/mol. This data indicates the slightly electron accepting character of the spacer unit from both the PAH moieties.

## Functionalized PAH-π-PAH systems: structure

The PAH-π-PAH systems show only minor variations in the electron density distribution at various parts of the system meaning that the donor-π-acceptor (D-π-A) character is very weak in PAH-π-PAH. Hence to force a more significant electronic rearrangement on the PAH moieties, an electron withdrawing group COOH and electron releasing group $NMe_2$ are introduced in the system. $NMe_2$ is introduced at the relatively more electron rich PAH portion (donor) while COOH is attached with the other PAH unit (acceptor). Seven such functionalized PAH-π-PAH systems (*f*_PAH-π-PAH) are considered here which showed the difference 0.5 kcal/mol between the $V_{min}$ values of the constituting PAH parts. These systems in abbreviated names are $f\_P_a1$-$C_z1$, $f\_T_a1$-$C_z1$, $f\_P_a1$-$C_a1$, $f\_T_a1$-$C_a1$, $f\_R_h1$-$C_a1$, $f\_P_a1$-$P_z1$ and $f\_T_a1$-$P_z1$ where *f* denotes the functionalization. The geometrical characteristics of planarity of PAH-π-PAH are retained in the functionalized systems. The optimized geometries of two designed *f*_PAH-π-PAH systems ($f\_T_a1$-$C_z1$ and $f\_R_h1$-$C_a1$) are given in Figure 8.

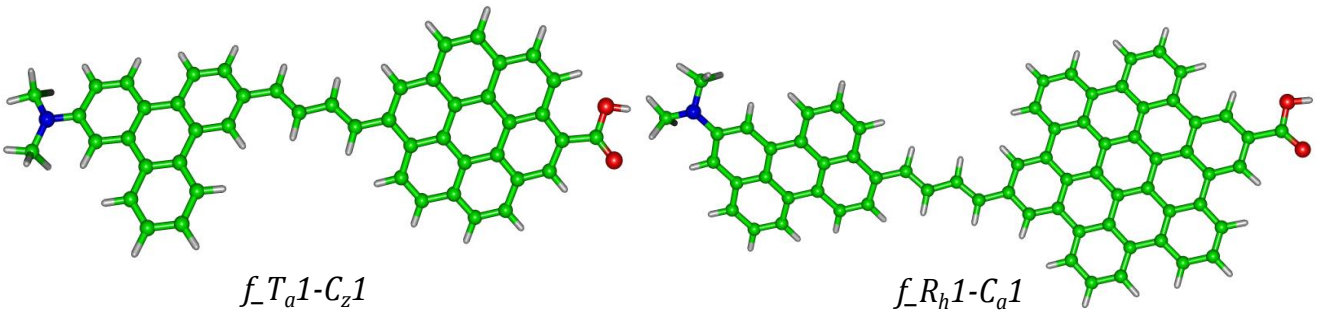


**Figure 8.** Geometry of representative functionalized PAH-π-PAH systems.

## Functionalized PAH-π-PAH systems: MESP analysis

The $V_{min}$ values on different parts of the systems (donor, acceptor and spacer) are given in Table 4. The MESP topography is significantly modified when the system is functionlized using electron donating and withdrawing groups.

**Table 4**. $V_{min}$ values on different parts of the functionalized PAH-π-PAH systems

| System | $V_{min}$D (kcal/mol) | $V_{min}$S (kcal/mol) | $V_{min}$A (kcal/mol) |
|---|---|---|---|
| *f_$P_a$1-$C_z$1* | -16.2 | -13.8 | -14.4 |
| *f_$T_a$1-$C_z$1* | -15.6 | -15.4 | -13.7 |
| *f_$P_a$1-$C_a$1* | -16.1 | -13.8 | -12.0 |
| *f_$T_a$1-$C_a$1* | -15.9 | -15.7 | -12.3 |
| *f_$R_h$1-$C_a$1* | -16.4 | -14.0 | -11.9 |
| *f_$P_a$1-$P_z$1* | -16.0 | -13.5 | -11.3 |
| *f_$T_a$1-$P_z$1* | -15.5 | -15.2 | -12.2 |

From the values it is clear that the electron density on the donor PAH is enhanced significantly compared to the non-functionalized systems. For example, $V_{min}$D on *$P_a$1-$C_a$1* is -13.4 kcal/mol, which is enhanced to a more negative -16.1 kcal/mol in *f_$P_a$1-$C_a$1*. It is also observed that in the acceptor part of PAH, the electron density shows only a moderate variation when functionalized; for example, $V_{min}$A on *$P_a$1-$C_a$1* of -12.5 kcal/mol is reduced to -12.0 kcal/mol for the functionalized *f_$P_a$1-$C_a$1* system. The MESP features confirm that the functionalized systems are more like a true D-π-A system. The visual representation of MESP for PAH-π-PAH (*$T_a$1-$C_a$1)* and *f*_PAH-π-PAH (*f_$T_a$1-$C_a$1)* systems is given in Figure 9, where the isosurface (in pink color) is plotted at the constant value of -10.0 kcal/mol and the position of the $V_{min}$ is marked using a black dot. The significant change in MESP distribution due to functionalization

is evident from the figure. See supporting Information for MESP isosurface for all other systems.

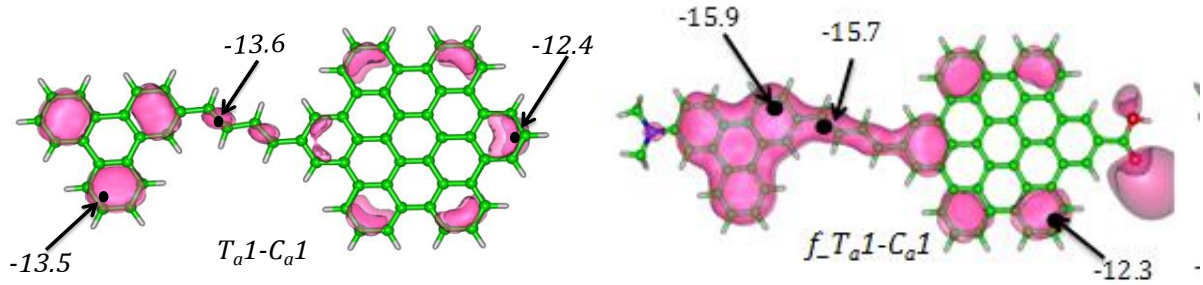


**Figure 9.** MESP features on *$T_a1$-$C_a1$* and *$f\_T_a1$-$C_a1$* systems, $V_{min}$ shown with a black dot.

## Frontier molecular orbital analysis

The change in the size and shape of any PAH system will contribute towards the HOMO-LUMO gap modulation.[40] The HOMO energy ($E_{HOMO}$), LUMO energy ($E_{LUMO}$) and the corresponding HOMO-LUMO energy gap (ΔE) of every systems are given in Table 5. The gradual tuning of ΔE with increase in number of rings is observed in each series. The data in Table 5 infer that the shape of the system and the zigzag or arm-chair periphery strongly influence the ΔE. Taking examples of *$C_a4$* having 73 rings, *$P_a4$* consisting of 57 rings, and *$R_h4$* made up of 14 rings, it is observed that ΔE is 0.88, 1.30 and 0.14 eV respectively. This proves that the shape of the PAH system is the most crucial in determining the electronic features of the systems. The peculiarity of *$R_hN$* type systems is evident from these values, as for very less number of rings, they exhibit very low ΔE than other systems. For example, the same ΔE of 2.05 eV is shown by *$R_h1$* made of 5 rings and *$C_z2$* made of 19 rings. The ΔE versus $n_\pi$ plot (Figure 10) show that *$C_zN$*, *$C_aN$*, *$P_zN$* and *$P_aN$* systems show a similar trend in the change in ΔE values, whereas the trends in the same for *$T_aN$* and *$R_hN$* systems are significantly varied

**Table 5.** HOMO, LUMO energies and HOMO-LUMO gap in eV

| System | $E_{HOMO}$ | $E_{LUMO}$ | $\Delta E$ | System | $E_{HOMO}$ | $E_{LUMO}$ | $\Delta E$ |
|---|---|---|---|---|---|---|---|
| *$C_z1$* | -5.19 | -2.11 | 3.09 | *$P_z1$* | -5.05 | -2.22 | 2.83 |
| *$C_z2$* | -4.75 | -2.70 | 2.05 | *$P_z2$* | -4.42 | -2.99 | 1.43 |
| *$C_z3$* | -4.51 | -3.05 | 1.46 | *$P_z3$* | -4.11 | -3.42 | 0.69 |
| *$C_z4$* | -4.36 | -3.29 | 1.07 | *$P_z4$* | -3.96 | -3.64 | 0.31 |
| *$C_a1$* | -5.00 | -2.34 | 2.65 | *$P_a1$* | -5.22 | -2.08 | 3.14 |
| *$C_a2$* | -4.58 | -2.90 | 1.68 | *$P_a2$* | -4.77 | -2.62 | 2.15 |
| *$C_a3$* | -4.51 | -3.13 | 1.38 | *$P_a3$* | -4.54 | -2.91 | 1.63 |
| *$C_a4$* | -4.28 | -3.39 | 0.88 | *$P_a4$* | -4.40 | -3.10 | 1.30 |
| *$R_h1$* | -4.69 | -2.64 | 2.05 | *$T_a1$* | -5.54 | -1.72 | 3.82 |
| *$R_h2$* | -4.20 | -3.19 | 1.01 | *$T_a2$* | -5.12 | -2.21 | 2.91 |
| *$R_h3$* | -3.94 | -3.51 | 0.43 | *$T_a3$* | -4.87 | -2.52 | 2.35 |
| *$R_h4$* | -3.83 | -3.69 | 0.14 | *$T_a4$* | -4.70 | -2.73 | 1.96 |

compared to the former. In *$T_aN$* and *$R_hN$* PAH systems, $\Delta E$ reduction is very high even for systems having less number of π-electrons.

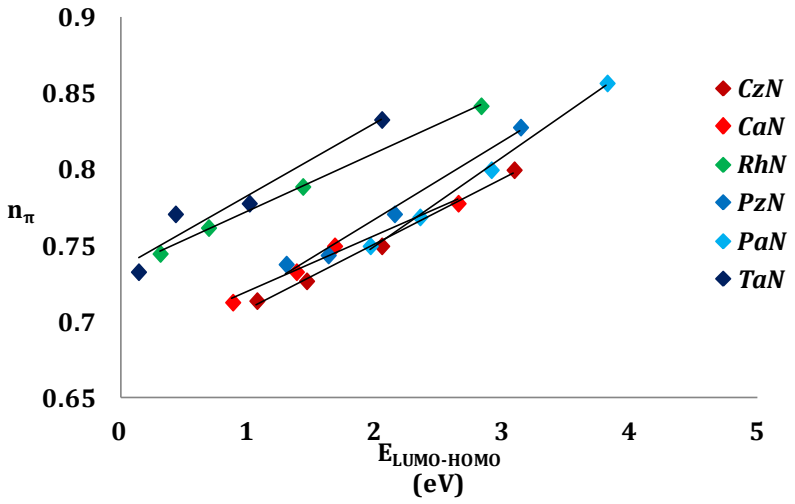


**Figure 10.** Graphs plotting $\Delta E$ and $n_\pi$ values on all the PAH systems.

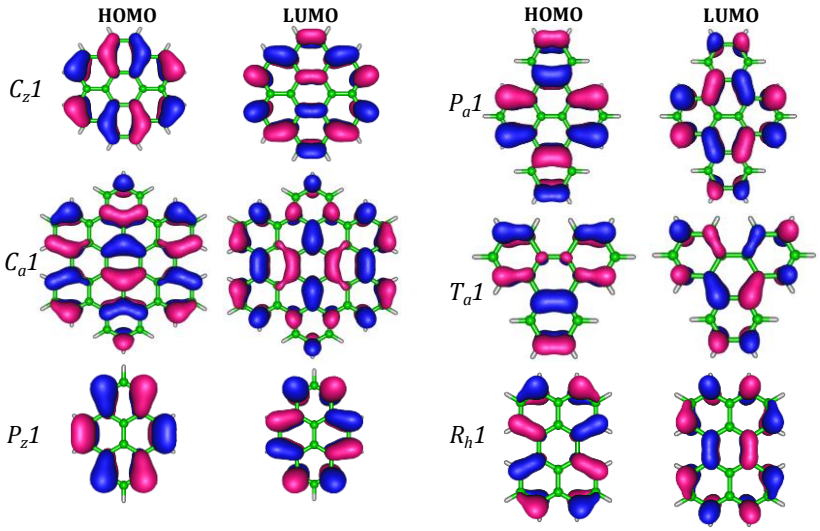


**Figure 11.** HOMO and LUMO of representative PAH systems.

The frontier molecular orbitals (FMOs) of all the systems are generated and a representative set including all the series are given in Figure 11 and the rest are given in the Supporting Information. The retention of the FMOs distribution pattern is seen in a series irrespective of the size change. In all the cases, the FMO is distribution is almost uniform throughout the carbon framework suggesting the extended delocalization which systematically lowers the ΔE.

For PAH-π-PAH systems, the energies $E_{HOMO}$, $E_{LUMO}$ and ΔE are given in Table 6. For all the systems the ΔE is in the range of 1.60 to 2.31 eV. The peculiarity of *$R_hN$* systems in lowering the energy gap is reflected in the designed systems. For example the PAH-π-PAH systems which have *$R_h1$* as structural component has the lowest ΔE values (1.60 eV for *$R_h1$-$C_a1$* and 1.61 eV for *$C_z1$-$R_h1$*). Rest of the systems show ΔE value above 2.00 eV. The highest ΔE 2.31 eV is observed for *$T_a1$-$P_z1$* system. The localization of HOMO on the donor PAH moiety and LUMO on the acceptor PAH moiety is mostly seen except for those connected with *$R_h1$*. In systems containing *$R_h1$*, the HOMO and LUMO distribution is mostly localised in the *$R_h1$* part. The visualization of HOMO and LUMO of *$P_z1$-$R_h1$* given in Figure 12 illustrates this feature (cf. Supp. Info.

**Table 6.** $E_{HOMO}$, $E_{LUMO}$ and $E_{LUMO-HOMO}$ for PAH-π-PAH systems.

| System | $E_{HOMO}$ (eV) | $E_{LUMO}$ (eV) | $\Delta E$ (eV) |
|---|---|---|---|
| *$C_z1$-$C_a1$* | -4.77 | -2.71 | 2.05 |
| *$C_z1$-$P_z1$* | -4.82 | -2.58 | 2.24 |
| *$P_a1$-$C_z1$* | -4.78 | -2.70 | 2.08 |
| *$T_a1$-$C_z1$* | -4.79 | -2.68 | 2.12 |
| *$C_z1$-$R_h1$* | -4.52 | -2.91 | 1.61 |
| *$P_z1$-$C_a1$* | -4.82 | -2.65 | 2.17 |
| *$P_a1$-$C_a1$* | -4.78 | -2.70 | 2.08 |
| *$T_a1$-$C_a1$* | -4.79 | -2.70 | 2.10 |
| *$R_h1$-$C_a1$* | -4.53 | -2.93 | 1.60 |
| *$P_a1$-$P_z1$* | -4.87 | -2.62 | 2.25 |
| *$T_a1$-$P_z1$* | -4.88 | -2.57 | 2.31 |
| *$P_z1$-$R_h1$* | -4.52 | -2.87 | 1.65 |
| *$T_a1$-$P_a1$* | -4.83 | -2.67 | 2.16 |
| *$P_a1$-$R_h1$* | -4.69 | -2.74 | 1.95 |
| *$T_a1$-$R_h1$* | -4.66 | -2.80 | 1.86 |

for FMOs of all the systems). Also in all the cases, the connecting diene has a clear influence on the MO population. In general, a clear demarcation between the donor and acceptor part of these molecules is not emerged from the HOMO and LUMO analysis.

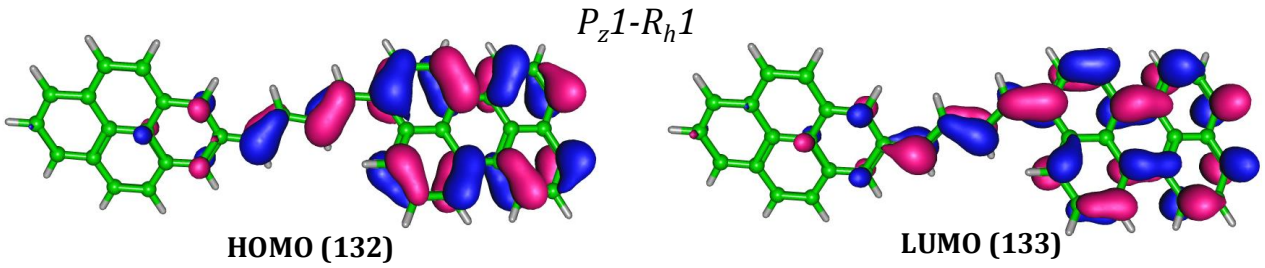


**Figure 12**. Frontier molecular orbitals of $P_z1$-$R_h1$ system

The values of FMO energies and band gap ΔE of all the *f*_PAH- π-PAH systems are given in Table 7. These systems possess lower ΔE in comparison with the PAH-π-PAH hydrocarbons. All the systems show ΔE lower than 2.00 eV. The $R_h1$ incorporated *f* _$R_h1$-$C_a1$ has the lowest ΔE 1.51 eV. As evident from the FMOs of *f*_$T_a1$-$C_z1$ (Figure 13), the HOMO is localised in the PAH region connected to the electron donating group, while the LUMO is localized towards the PAH connected with the electron withdrawing group. These systems are expected to show the characteristic charge-transfer absorption features typical for a D-π-A system.

**Table 7**. $E_{HOMO}$, $E_{LUMO}$ and ΔE for functionalized PAH-π-PAH systems.

| System | $E_{HOMO}$ (eV) | $E_{LUMO}$ (eV) | ΔE (eV) |
|---|---|---|---|
| *f* _$P_a1$-$C_z1$ | -4.65 | -2.79 | 1.86 |
| *f* _$T_a1$-$C_z1$ | -4.54 | -2.70 | 1.84 |
| *f* _$P_a1$-$C_a1$ | -4.66 | -2.76 | 1.90 |
| *f* _$T_a1$-$C_a1$ | -4.54 | -2.71 | 1.83 |
| *f* _$R_h1$-$C_a1$ | -4.41 | -2.90 | 1.51 |
| *f* _$P_a1$-$P_z1$ | -4.66 | -2.72 | 1.94 |
| *f* _$T_a1$-$P_z1$ | -4.57 | -2.61 | 1.96 |

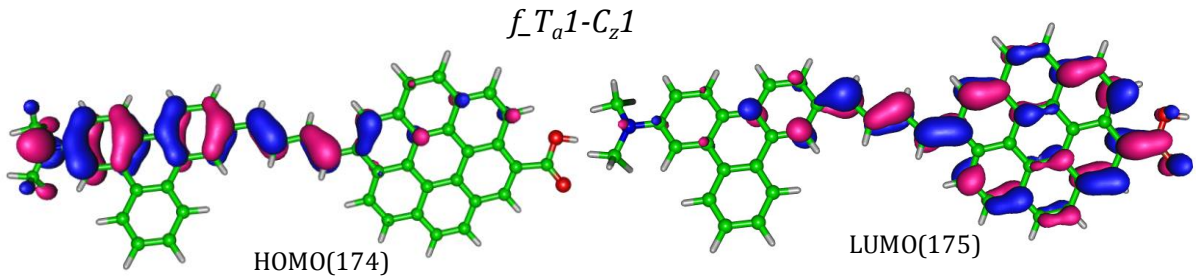


**Figure 13**. Frontier molecular orbitals of *f_Ta1-Cz1* system.

## Optical properties

The calculated optical properties include absorption maxima ($\lambda_{max}$), oscillator strength (*f*), light harvesting efficiency (LHE), excitation energy, and the most prominent FMO contribution. Tuning of these properties is assessed on the basis of the size and shape of the systems as well as the number of benzenoid rings present.

The optical properties of the PAH systems are given in Table 8 and Table 9. Table 8 lists the most prominent $\lambda_{max}$ values and the MO contribution corresponding to it. Although, the transitions other than the HOMO-LUMO can give rise to absorption maxima values of different strengths, the one corresponding to HOMO-LUMO, the longest wavelength absorption need not be the most prominent one. For the absorption process in *CzN* and *CaN* series, the prominent the FMOs with high percentage contributions is in the range 32 – 48 %, an exception being the *C4N* having HOMO → LUMO percentage contribution of 5% only. In all other systems, the inner orbital contributions are also significant.

The absorption spectra of representative PAH systems are illustrated in Figure 14. For all the systems in *CzN*, single $\lambda_{max}$ values are observed with an exception *Cz4*. For a comparison with experimentally available absorption data, the value 300 nm[66] in the case of *Cz1* (coronene) is matched with the calculated value at M06L/6-31+G(d) level 317 nm. For *Cz2,* the $\lambda_{max}$ is 469 nm, whereas for *Cz3,* the value is 648 nm. The largest system *Cz4*shows $\lambda_{max}$ at 865 nm along with weak absorptions in the region of

**Table 8.** Absorption maxima and corresponding MO contribution for the most prominent transition in PAH systems

| System | $\lambda_{max}$ (nm) | MO contribution (%) | | System | $\lambda_{max}$ (nm) | MO contribution (%) | |
|---|---|---|---|---|---|---|---|
| *$C_z1$* | 317 | HOMO → LUMO | 44 | *$P_a1$* | 234 | HOMO-2 → LUMO+3 | 52 |
| *$C_z2$* | 469 | HOMO → LUMO | 32 | *$P_a2$* | 437 | HOMO → LUMO+1 | 50 |
| *$C_z3$* | 648 | HOMO → LUMO | 46 | *$P_a3$* | 561 | HOMO → LUMO+1 | 50 |
| *$C_z4$* | 865 | HOMO → LUMO | 46 | *$P_a4$* | 686 | HOMO → LUMO+1 | 50 |
| *$C_a1$* | 397 | HOMO → LUMO | 46 | *$T_a1$* | 258 | HOMO-2 → LUMO | 51 |
| *$C_a2$* | 619 | HOMO → LUMO | 39 | *$T_a2$* | 362 | HOMO → LUMO | 41 |
| *$C_a3$* | 754 | HOMO → LUMO | 48 | *$T_a3$* | 445 | HOMO → LUMO+1 | 41 |
| *$C_a4$* | 1122 | HOMO → LUMO | 5 | *$T_a4$* | 530 | HOMO → LUMO+1 | 39 |
| *$P_z1$* | 235 | HOMO-1 → LUMO+1 | 79 | *$R_h1$* | 463 | HOMO → LUMO | 98 |
| *$P_z2$* | 569 | HOMO → LUMO | 95 | *$R_h2$* | 321 | HOMO → LUMO+5 | 52 |
| *$P_z3$* | 491 | HOMO-1 → LUMO+1 | 77 | *$R_h3$* | 324 | HOMO → LUMO+7 | 61 |
| *$P_z4$* | 756 | HOMO-1 → LUMO+1 | 67 | *$R_h4$* | 375 | HOMO → LUMO+5 | 40 |

600- 640 nm. *$C_a1$* system (hexabenzocoronene) has $\lambda_{max}$ at 397 nm and a shoulder at 341 nm. The experimental $\lambda_{max}$ for this system is centred around 350nm.[67] *$C_a2$* shows $\lambda_{max}$ at 619 nm and a shoulder at 413nm. *$C_a3$* has $\lambda_{max}$ at 754 and shoulder at 552 nm, whereas the largest system analysed *$C_a4$* has $\lambda_{max}$ at 1122 nm and shoulder at 764 nm.

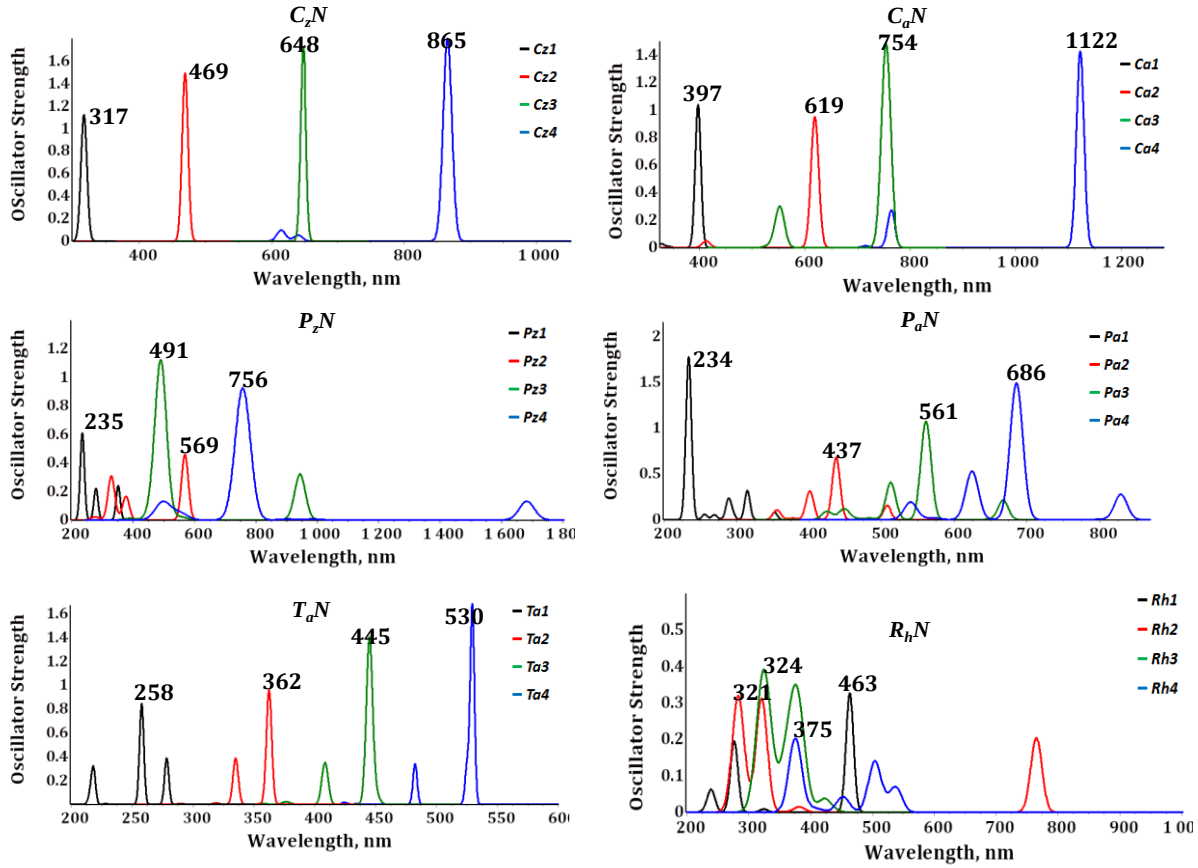


**Figure 14.** Absorption spectra of PAH systems at M06L/6-31+G(d) level of theory.

*$P_z1$* is pyrene which has an experimental $\lambda_{max}$ around 250 nm,[68] and the calculated value 235 nm agree well with this. Also it shows minor peaks at 352 nm and 279 nm. For *$P_z2$*, $\lambda_{max}$ values are at 329, 377 and 569 nm. *$P_z3$* system absorbs strongly at 491 nm and weakly at 945 nm. The largest system *$P_z4$* absorbs strongly at 756 nm, while the weakly absorbing peaks are observed at 495 and 1680 nm. For *$P_aN$* series, predominantly four sets of $\lambda_{max}$ can be visualised. *$P_a1$* has $\lambda_{max}$ at 234, 289 and 315 nm. For *$P_a2$*, the strongest absorption occurs at 437 nm along with minor peaks at 355, 401 and 508 nm. For *$P_a3$*, $\lambda_{max}$ are at 668, 561, 512 and 449 nm. *$P_a4$* system absorbs strongly in the 686 nm and weakly in the regions of wavelength 829, 625 and 540 nm. Triphenylene which is denoted as *$T_a1$*, has the reported experimental $\lambda_{max}$ in the region of 250 nm.[69] This value is in agreement with the calculated value 258 nm. It also shows minor peaks at $\lambda_{max}$ 278 and 218 nm. *$T_a2$* has $\lambda_{max}$ at 362 and 335 nm while *$T_a3$* show

peaks at 451 and 409 nm. In the case of $T_a4$, $\lambda_{max}$ are at 530 and 483 nm. Perylene molecule $R_h1$ has an experimental $\lambda_{max}$ ~430 nm in methanol[70] which is close to the theoretical value 463 nm obtained here. Other $\lambda_{max}$ of $R_h1$ are 229 and 277 nm. $R_h2$ has mainly three $\lambda_{max}$, *viz*. 284, 321 and 765 nm. For $R_h3$ systems, $\lambda_{max}$ are observed at 324, 380 and 1297 nm. For the largest studied stystem $R_h4$, $\lambda_{max}$ are observed at 375, 504 and 2505 nm.

The light harvesting efficiency (LHE) of the PAH systems increases as the number of rings increases. As evident from Table 9, the energy requirement for the vertical excitation declines with the size enhancement. Most of the systems have LHE in the range from 0.755 to 0.981. LHE of $T_aN$ systems is in the range 0.6 to 0.8. For $R_hN$ systems, LHE is the lowest. From the analysis of vertical excitation energy, the rectangular systems show the lowest value.

The effect of periphery shape is highly influential on the absorption characteristics of a PAH molecules. For example, $R_h4$ system having only 14 fused benzenoid shows $\lambda_{max}$ 2505 nm which is very large compared to the $\lambda_{max}$ of other much larger systems.

Table 10 gives the optical features of PAH-π-PAH systems. The absorption maxima values in the range of 433 nm to 630 nm are possible for these systems. The highest $\lambda_{max}$ is observed for the $R_h1$-$C_a1$ which is at 630 nm and the least $\lambda_{max}$ of 433 nm is seen for $T_a1$-$P_z1$ system. The absorption in the visible region of solar spectrum is attained for all the systems, which can be highly beneficial in solar energy harvesting applications.

In most of the systems, the prominent absorption having the highest oscillator strength is the one corresponding to HOMO→LUMO transition. The oscillator strength of all the designed PAH-π-PAH systems is in the range 0.80 to 1.95. Oscillator strength being a direct measure of the LHE, the changes in its values is reflected in the LHE. The $T_a1$-$P_z1$ system has maximum LHE of 0.989 with the oscillator strength of 1.957, and the

**Table 9.** Oscillator strength, light harvesting efficiency and excitation energy of PAH systems

| System | Oscillator strength | LHE | Excitation energy (eV) | System | Oscillator strength | LHE | Excitation energy (eV) |
|---|---|---|---|---|---|---|---|
| *$C_z1$* | 0.562 | 0.726 | 3.07 | *$P_a1$* | 1.726 | 0.981 | 3.48 |
| *$C_z2$* | 0.747 | 0.821 | 2.04 | *$P_a2$* | 0.681 | 0.792 | 2.44 |
| *$C_z3$* | 0.864 | 0.863 | 1.45 | *$P_a3$* | 1.073 | 0.916 | 1.86 |
| *$C_z4$* | 0.901 | 0.875 | 1.07 | *$P_a4$* | 1.495 | 0.968 | 1.49 |
| *$C_a1$* | 0.520 | 0.698 | 2.65 | *$T_a1$* | 0.423 | 0.622 | 3.81 |
| *$C_a2$* | 0.477 | 0.666 | 1.68 | *$T_a2$* | 0.480 | 0.669 | 2.91 |
| *$C_a3$* | 0.742 | 0.819 | 1.39 | *$T_a3$* | 0.702 | 0.802 | 2.34 |
| *$C_a4$* | 0.714 | 0.807 | 0.88 | *$T_a4$* | 0.838 | 0.855 | 1.96 |
| *$P_z1$* | 0.610 | 0.755 | 3.53 | *$R_h1$* | 0.327 | 0.529 | 2.68 |
| *$P_z2$* | 0.460 | 0.653 | 2.18 | *$R_h2$* | 0.311 | 0.512 | 1.08 |
| *$P_z3$* | 1.079 | 0.917 | 1.29 | *$R_h3$* | 0.381 | 0.584 | 0.96 |
| *$P_z4$* | 0.926 | 0.881 | 0.66 | *$R_h4$* | 0.201 | 0.370 | 0.49 |

least efficient in light harvesting is *$P_a1$-$R_h1$* with a LHE 0.802 and oscillator strength 0.703. Vertical excitation energies of all the designed systems are in the range of 2.0 – 2.6 eV. Systems having high LHE and low excitation energy are ideal for photonic applications. The most prominent MO transition is HOMO $\rightarrow$ LUMO (62 - 92 %) for all the PAH-π-PAH systems, except *$T_a1$-$P_z1$*, *$T_a1$-$R_h1$*, and *$P_a1$-$R_h1$*. (The absorption spectra of all the systems are given in Supp. Info.)

Compared to PAH-π-PAH, the functionalized PAH-π-PAH systems show significantly more red-shifted $\lambda_{max}$ (Table 11). For example, *$T_a1$-$C_a1$* has $\lambda_{max}$ 529 nm, whereas *f_$T_a1$-$C_a1$* has 634 nm. The light harvesting efficiency decreased for the functionalized

systems, an exception is *f_Pa1-Pz1*, where the LHE is enhanced to 0.903 from 0.882 observed for *Pa1-Pz1*. The vertical excitation energy of *f*_PAH-π-PAH is significantly lowered compared to PAH-π-PAH. Maximum change in vertical excitation energy is observed for *f_Pa1-Pz1*, which has excitation energy 1.88 eV whereas the same for *Pa1-Pz1* system is 2.53 eV.

**Table 10**. Optical data for PAH-π-PAH type systems

| System | $\lambda_{max}$ (nm) | MO contribution (%) | | Oscillator strength (*f*) | LHE | Excitation energy (eV) |
|---|---|---|---|---|---|---|
| *Cz1-Ca1* | 542 | HOMO→ LUMO | 87 | 1.218 | 0.940 | 2.29 |
| *Cz1-Pz1* | 475 | HOMO→ LUMO | 72 | 1.006 | 0.901 | 2.54 |
| *Pa1-Cz1* | 506 | HOMO→ LUMO | 90 | 1.543 | 0.971 | 2.45 |
| *Ta1-Cz1* | 495 | HOMO→ LUMO | 92 | 1.478 | 0.967 | 2.50 |
| *Cz1-Rh1* | 610 | HOMO→ LUMO | 90 | 1.357 | 0.956 | 2.03 |
| *Pz1-Ca1* | 518 | HOMO→ LUMO | 79 | 0.821 | 0.849 | 2.39 |
| *Pa1-Ca1* | 532 | HOMO→ LUMO | 85 | 1.101 | 0.921 | 2.33 |
| *Ta1-Ca1* | 529 | HOMO→ LUMO | 85 | 1.010 | 0.902 | 2.34 |
| *Rh1-Ca1* | 630 | HOMO→ LUMO | 82 | 1.413 | 0.961 | 1.97 |
| *Pa1-Pz1* | 467 | HOMO → LUMO | 61 | 0.928 | 0.882 | 2.53 |
| *Ta1-Pz1* | 451 | HOMO→ LUMO+1 | 41 | 1.957 | 0.989 | 2.57 |
| *Pz1-Rh1* | 578 | HOMO→ LUMO | 95 | 1.317 | 0.952 | 2.14 |
| *Ta1-Pa1* | 480 | HOMO→ LUMO | 79 | 1.495 | 0.968 | 2.58 |
| *Pa1-Rh1* | 478 | HOMO-1→ LUMO | 30 | 0.703 | 0.802 | 2.20 |
| *Ta1-Rh1* | 468 | HOMO→ LUMO+1 | 50 | 1.189 | 0.935 | 2.18 |

**Table 11.** Optical data of all the functionalized PAH-π-PAH systems.

| System | $\lambda_{max}$ (nm) | MO contribution (%) | Oscillator strength(f) | LHE | Excitation energy (eV) |
|---|---|---|---|---|---|
| *f_$P_a$1-$C_a$1* | 546 | HOMO-1→ LUMO 75 | 0.836 | 0.854 | 1.92 |
| *f_$T_a$1-$C_z$1* | 626 | HOMO→ LUMO 87 | 0.695 | 0.798 | 1.98 |
| *f_$P_a$1-$C_a$1* | 546 | HOMO-1→ LUMO 75 | 0.836 | 0.854 | 1.92 |
| *f_$T_a$1-$C_a$1* | 634 | HOMO→ LUMO 90 | 0.887 | 0.870 | 1.96 |
| *f_$R_h$1-$C_a$1* | 708 | HOMO→ LUMO 67 | 0.580 | 0.737 | 1.75 |
| *f_$P_a$1-$P_z$1* | 552 | HOMO-1→ LUMO 55 | 1.011 | 0.903 | 1.88 |
| *f_$T_a$1-$P_z$1* | 570 | HOMO→ LUMO 81 | 0.809 | 0.845 | 2.18 |

# Conclusions

The design and study of polycyclic aromatic hydrocarbons (PAHs) or graphene nanoflakes has significance in the photosciences and photonics fields due to the excellent photonic and optoelectronic properties exhibited by them. Here several PAH systems are designed by changing the number of constituting rings, the shape of periphery and the geometry of the whole molecule. Circular, parallelogram, triangular and rectangular shaped PAHs has been designed and studied. DFT calculations at M06L/6-31+G(d) level have been carried out on the PAH systems to theoretically analyse the absorption properties together with electronic properties. In all the molecules, the frontier molecular orbitals analysis is carried out for the better understanding of reactivity and electronic features. In all the different shaped PAHs, there is direct increase in the absorption maxima with increase in number of carbon atoms. This phenomenon is obvious because as the number of carbon atoms increases there is extending of conjugation in the structure, which shifts the absorption

maxima to greater wavelengths. As conjugation increases, the HOMO-LUMO gap gets shortened, thus less energy is required to cause the electronic transitions. As a result of which, the corresponding wavelength gets enhanced. One important feature that was observed is the dependence of shape and periphery geometry on the optical and electronic features of PAH systems. For molecules that are composed of same number of benzene rings, the electronic structure, features, and optical properties are distinctly different. As a direct result, for PAHs having same number of carbon atoms, the electron density can be different if their shape is differed. This paved the design and studies on D-π-A type systems connecting two PAH units via a conjugated π-system. The theoretical calculations on a set of such designed systems are done, which enhanced the possibility of developing D-π-A system as the PAH moieties showed different electronic features compared to each other. However, the donor-acceptor type feature is mildly present in the designed PAH-π-PAH systems and a quantification of the electronic feature is done with the help of $V_{min}$ values, which were different on different parts of the same system. Introduction of electron donating and withdrawing groups on these designed systems is done for further enhancement of electronic and optical features to improve the donor-acceptor character. The frontier molecular orbital analysis also reinforced the difference in the observed electronic features. The functionalization results in the minor lowering of the light harvesting efficiency and excitation energy for all the analysed systems.

Armchair edged PAH system are found to be more resonance stabilised, which is supported by the Clar's aromatic sextet like MESP isosurface arrangement in the entire structure. For zigzag periphery systems, the electron cloud is localised more towards the edges and these classes of systems might be very useful for donor-acceptor type electronic applications. Rectangular shaped PAH systems having both armchair and zigzag edges in same molecule are electronically very dense which has a characteristic

very low HOMO-LUMO gap even when number of rings constituting is less. This effect is verified by comparing with other systems of much higher number of constituting rings. In summary, the theoretical study on PAH, PAH-π-PAH and *f*_PAH-π-PAH systems provide new insight on the design and development of efficient light harvesting molecules that are derived from graphene nanoflakes of different sizes and shapes.

## Supporting Information

MESP figures, HOMO and LUMO representations, Absorption spectra, and Optimized nuclear coordinates of all the structures.

## Acknowledgment

This work is supported by the SERB funding through the project GAP139739.

## References

(1) Novoselov, K. S.; Geim, A. K.; Morozov, S. V.; Jiang, D.; Zhang, Y.; Dubonos, S. V.; Grigorieva, I. V.; Firsov, A. A. Electric Field Effect in Atomically Thin Carbon Films. *Science* **2004**, *306*, 666.

(2) Wallace, P. R. The Band Theory of Graphite. *Phys. Rev.* **1947**, *71*, 622-634.

(3) Watson, M. D.; Fechtenkötter, A.; Müllen, K. Big Is Beautiful−“Aromaticity” Revisited from the Viewpoint of Macromolecular and Supramolecular Benzene Chemistry. *Chem. Rev.* **2001**, *101*, 1267-1300.

(4) Pisula, W.; Feng, X.; Müllen, K. Charge-Carrier Transporting Graphene-Type Molecules. *Chemistry of Materials* **2011**, *23*, 554-567.

(5) Geim, A. K.; MacDonald, A. H. Graphene: Exploring carbon flatland. *Phys. Today* **2007**, *60*, 35-41.

(6) Novoselov, K. S. Graphene: Materials in the Flatland (Nobel Lecture). *Angew. Chem. Int. Ed.* **2011**, *50*, 6986-7002.

(7) Casiraghi, C.; Hartschuh, A.; Lidorikis, E.; Qian, H.; Harutyunyan, H.; Gokus, T.; Novoselov, K. S.; Ferrari, A. C. Rayleigh Imaging of Graphene and Graphene Layers. *Nano Lett.* **2007**, *7*, 2711-2717.

(8) Blake, P.; Hill, E. W.; Neto, A. H. C.; Novoselov, K. S.; Jiang, D.; Yang, R.; Booth, T. J.; Geim, A. K. Making graphene visible. *Appl. Phys. Lett.* **2007**, *91*, 063124.

(9) Nair, R. R.; Blake, P.; Grigorenko, A. N.; Novoselov, K. S.; Booth, T. J.; Stauber, T.; Peres, N. M. R.; Geim, A. K. Fine Structure Constant Defines Visual Transparency of Graphene. *Science* **2008**, *320*, 1308.

(10) Hasan, T.; Sun, Z.; Wang, F.; Bonaccorso, F.; Tan, P. H.; Rozhin, A. G.; Ferrari, A. C. Nanotube–Polymer Composites for Ultrafast Photonics. *Adv. Mater.* **2009**, *21*, 3874-3899.

(11) Sun, Z.; Hasan, T.; Torrisi, F.; Popa, D.; Privitera, G.; Wang, F.; Bonaccorso, F.; Basko, D. M.; Ferrari, A. C. Graphene Mode-Locked Ultrafast Laser. *ACS Nano* **2010**, *4*, 803-810.

(12) Stöhr, R. J.; Kolesov, R.; Pflaum, J.; Wrachtrup, J. Fluorescence of laser-created electron-hole plasma in graphene. *Phys. Rev. B* **2010**, *82*, 121408.

(13) Gokus, T.; Nair, R. R.; Bonetti, A.; Böhmler, M.; Lombardo, A.; Novoselov, K. S.; Geim, A. K.; Ferrari, A. C.; Hartschuh, A. Making Graphene Luminescent by Oxygen Plasma Treatment. *ACS Nano* **2009**, *3*, 3963-3968.

(14) Eda, G.; Lin, Y.-Y.; Mattevi, C.; Yamaguchi, H.; Chen, H.-A.; Chen, I. S.; Chen, C.-W.; Chhowalla, M. Blue Photoluminescence from Chemically Derived Graphene Oxide. *Adv. Mater.* **2010**, *22*, 505-509.

(15) Sun, X.; Liu, Z.; Welsher, K.; Robinson, J. T.; Goodwin, A.; Zaric, S.; Dai, H. Nano-graphene oxide for cellular imaging and drug delivery. *Nano Res.* **2008**, *1*, 203-212.

(16) Luo, Z.; Vora, P. M.; Mele, E. J.; Johnson, A. T. C.; Kikkawa, J. M. Photoluminescence and band gap modulation in graphene oxide. *Appl. Phys. Lett.* **2009**, *94*, 111909.

(17) Bonaccorso, F.; Sun, Z.; Hasan, T.; Ferrari, A. C. Graphene photonics and optoelectronics. *Nat. Photon.* **2010**, *4*, 611-622.

(18) Geim, A. K.; Novoselov, K. S. The rise of graphene. *Nat. Mater.* **2007**, *6*, 183-191.

(19) Snook, I.; Barnard, A. In *Physics and Applications of Graphene - Theory.*; Mikhailov, S., Ed.; InTech.: Rijeka, Croatia, 2011, p 277-302.

(20) Müller, S.; Müllen, K. Expanding benzene to giant graphenes: towards molecular devices. *Phil. Trans. R. Soc. A* **2007**, *365*, 1453-1472.

(21) Barnard, A. S.; Snook, I. K. Modelling the role of size, edge structure and terminations on the electronic properties of graphene nano-flakes. *Model. Simul. Mater. Sci. Eng.* **2011**, *19*, 054001.

(22) Wu, J.; Pisula, W.; Müllen, K. Graphenes as Potential Material for Electronics. *Chem. Rev.* **2007**, *107*, 718-747.

(23) Narita, A.; Wang, X.-Y.; Feng, X.; Mullen, K. New advances in nanographene chemistry. *Chem. Soc. Rev.* **2015**, *44*, 6616-6643.

(24) Rieger, R.; Müllen, K. Forever young: polycyclic aromatic hydrocarbons as model cases for structural and optical studies. *J. Phys. Org. Chem.* **2010**, *23*, 315-325.

(25) Kim, S.; Hwang, S. W.; Kim, M.-K.; Shin, D. Y.; Shin, D. H.; Kim, C. O.; Yang, S. B.; Park, J. H.; Hwang, E.; Choi, S.-H.; Ko, G.; Sim, S.; Sone, C.; Choi, H. J.;

Bae, S.; Hong, B. H. Anomalous Behaviors of Visible Luminescence from Graphene Quantum Dots: Interplay between Size and Shape. *ACS Nano* **2012**, *6*, 8203-8208.

(26) Bacon, M.; Bradley, S. J.; Nann, T. Graphene Quantum Dots. *Part. Part. Syst. Charact.* **2014**, *31*, 415-428.

(27) Pelloni, S.; Lazzeretti, P. Polygonal current models for polycyclic aromatic hydrocarbons and graphene sheets of various shapes. *J. Comput. Chem.* **2018**, *39*, 21-34.

(28) Lin, C. K. Theoretical study of nitrogen-doped graphene nanoflakes: Stability and spectroscopy depending on dopant types and flake sizes. *J. Comput. Chem.* **2018**, *39*, 1387-1397.

(29) Siegmann, K.; Sattler, K. Formation mechanism for polycyclic aromatic hydrocarbons in methane flames. *J. Chem. Phys.* **2000**, *112*, 698-709.

(30) Güçlü, A. D.; Hawrylak, P. Optical control of magnetization and spin blockade in graphene quantum dots. *Phys. Rev. B* **2013**, *87*, 035425.

(31) Kuc, A.; Heine, T.; Seifert, G. Structural and electronic properties of graphene nanoflakes. *Phys. Rev. B* **2010**, *81*, 085430.

(32) Kosimov, D. P.; Dzhurakhalov, A. A.; Peeters, F. M. Carbon clusters: From ring structures to nanographene. *Phys. Rev. B* **2010**, *81*, 195414.

(33) Alessandra, R.; Charles W. Bauschlicher, Jr.; Christiaan, B.; Alexander, G. G. M. T.; Louis, J. A. The Infrared Spectroscopy of Compact Polycyclic Aromatic Hydrocarbons Containing up to 384 Carbons. *Astrophys. J.* **2012**, *754*, 75.

(34) Lu, P.; Zhang, Z.; Woo, C. H.; Guo, W. Nonlinear–Linear Transition of Magnetoelectric Effect in Magnetic Graphene Nanoflakes on Substrates. *J. Phys. Chem. C* **2012**, *116*, 626-631.

(35) Hongqing, S.; Amanda, S. B.; Ian, K. S. Modelling the role of size, edge structure and terminations on the electronic properties of trigonal graphene nanoflakes. *Nanotechnology* **2012**, *23*, 065707.

(36) Suresh, C. H.; Gadre, S. R. Clar's Aromatic Sextet Theory Revisited via Molecular Electrostatic Potential Topography. *J. Org. Chem.* **1999**, *64*, 2505-2512.

(37) Vijayalakshmi, K. P.; Suresh, C. H. Pictorial representation and validation of Clar's aromatic sextet theory using molecular electrostatic potentials. *New J. Chem.* **2010**, *34*, 2132-2138.

(38) Suresh, C. H.; Ajitha, M. J. DFT Prediction of Multitopic N-Heterocyclic Carbenes Using Clar's Aromatic Sextet Theory. *J. Org. Chem.* **2013**, *78*, 3918-3924.

(39) Vijayalakshmi, K. P.; Suresh, C. H. Theoretical studies on the carcinogenicity of polycyclic aromatic hydrocarbons. *J. Comput. Chem.* **2008**, *29*, 1808-1817.

(40) Mandal, B.; Sarkar, S.; Sarkar, P. Exploring the electronic structure of graphene quantum dots. *J. Nanopart. Res.* **2012**, *14*, 1317.

(41) Wohner, N.; Lam, P.; Sattler, K. Energetic stability of graphene nanoflakes and nanocones. *Carbon* **2014**, *67*, 721-735.

(42) Vázquez de Parga, A. L.; Calleja, F.; Borca, B.; Passeggi, M. C. G.; Hinarejos, J. J.; Guinea, F.; Miranda, R. Periodically Rippled Graphene: Growth and Spatially Resolved Electronic Structure. *Phys. Rev. Lett.* **2008**, *100*, 056807.

(43) Geng, D.; Wu, B.; Guo, Y.; Huang, L.; Xue, Y.; Chen, J.; Yu, G.; Jiang, L.; Hu, W.; Liu, Y. Uniform hexagonal graphene flakes and films grown on liquid copper surface. *Proc. Nat. Acad. Sci. USA* **2012**, *109*, 7992-7996.

(44) Helveg, S.; Lopez-Cartes, C.; Sehested, J.; Hansen, P. L.; Clausen, B. S.; Rostrup-Nielsen, J. R.; Abild-Pedersen, F.; Norskov, J. K. Atomic-scale imaging of carbon nanofibre growth. *Nature* **2004**, *427*, 426-429.

(45) Samorí, P.; Severin, N.; Simpson, C. D.; Müllen, K.; Rabe, J. P. Epitaxial Composite Layers of Electron Donors and Acceptors from Very Large Polycyclic Aromatic Hydrocarbons. *J. Am. Chem. Soc.* **2002**, *124*, 9454-9457.

(46) Khan, U.; O'Neill, A.; Porwal, H.; May, P.; Nawaz, K.; Coleman, J. N. Size selection of dispersed, exfoliated graphene flakes by controlled centrifugation. *Carbon* **2012**, *50*, 470-475.

(47) Güttinger, J.; Molitor, F.; Stampfer, C.; Schnez, S.; Jacobsen, A.; Dröscher, S.; Ihn, T.; Ensslin, K. Transport through graphene quantum dots. *Rep. Prog. Phys.* **2012**, *75*, 126502.

(48) Barreiro, A.; van der Zant, H. S. J.; Vandersypen, L. M. K. Quantum Dots at Room Temperature Carved out from Few-Layer Graphene. *Nano Lett.* **2012**, *12*, 6096-6100.

(49) Wang, J.; Manga, K. K.; Bao, Q.; Loh, K. P. High-Yield Synthesis of Few-Layer Graphene Flakes through Electrochemical Expansion of Graphite in Propylene Carbonate Electrolyte. *J. Am. Chem. Soc.* **2011**, *133*, 8888-8891.

(50) Han, M. Y.; Özyilmaz, B.; Zhang, Y.; Kim, P. Energy Band-Gap Engineering of Graphene Nanoribbons. *Phys. Rev. Lett.* **2007**, *98*, 206805.

(51) Shang, N. G.; Papakonstantinou, P.; McMullan, M.; Chu, M.; Stamboulis, A.; Potenza, A.; Dhesi, S. S.; Marchetto, H. Catalyst-Free Efficient Growth, Orientation and Biosensing Properties of Multilayer Graphene Nanoflake Films with Sharp Edge Planes. *Adv. Funct. Mater.* **2008**, *18*, 3506-3514.

(52) Nakajima, T.; Shintani, K. Molecular dynamics study of energetics of graphene flakes. *J. Appl. Phys.* **2009**, *106*, 114305.

(53) Stein, S. E.; Brown, R. L. .pi.-Electron properties of large condensed polyaromatic hydrocarbons. *J. Am. Chem. Soc.* **1987**, *109*, 3721-3729.

(54) Akola, J.; Heiskanen, H. P.; Manninen, M. Edge-dependent selection rules in magic triangular graphene flakes. *Phys. Rev. B* **2008**, *77*, 193410.

(55) Balaban, A. T. Using Clar sextets for two- and three-dimensional aromatic systems. *Phys. Chem. Chem. Phys.* **2011**, *13*, 20649-20658.

(56) Baldoni, M.; Sgamellotti, A.; Mercuri, F. Electronic properties and stability of graphene nanoribbons: An interpretation based on Clar sextet theory. *Chem. Phys. Lett.* **2008**, *464*, 202-207.

(57) Graver, J. E. Kekulé structures and the face independence number of a fullerene. *Eur. J. Comb.* **2007**, *28*, 1115-1130.

(58) Frisch, M. J.; Trucks, G. W.; Schlegel, H. B.; Scuseria, G. E.; Robb, M. A.; Cheeseman, J. R.; Scalmani, G.; Barone, V.; Petersson, G. A.; Nakatsuji, H.; Li, X.; Caricato, M.; Marenich, A. V.; Bloino, J.; Janesko, B. G.; Gomperts, R.; Mennucci, B.; Hratchian, H. P.; Ortiz, J. V.; Izmaylov, A. F.; Sonnenberg, J. L.; Williams; Ding, F.; Lipparini, F.; Egidi, F.; Goings, J.; Peng, B.; Petrone, A.; Henderson, T.; Ranasinghe, D.; Zakrzewski, V. G.; Gao, J.; Rega, N.; Zheng, G.; Liang, W.; Hada, M.; Ehara, M.; Toyota, K.; Fukuda, R.; Hasegawa, J.; Ishida, M.; Nakajima, T.; Honda, Y.; Kitao, O.; Nakai, H.; Vreven, T.; Throssell, K.; Montgomery Jr., J. A.; Peralta, J. E.; Ogliaro, F.; Bearpark, M. J.; Heyd, J. J.; Brothers, E. N.; Kudin, K. N.; Staroverov, V. N.; Keith, T. A.; Kobayashi, R.; Normand, J.; Raghavachari, K.; Rendell, A. P.; Burant, J. C.; Iyengar, S. S.; Tomasi, J.; Cossi, M.; Millam, J. M.; Klene, M.; Adamo, C.; Cammi, R.; Ochterski, J. W.; Martin, R. L.; Morokuma, K.; Farkas, O.; Foresman, J. B.; Fox, D. J. Wallingford, CT, 2016.

(59) Remya, K.; Suresh, C. H. Which density functional is close to CCSD accuracy to describe geometry and interaction energy of small noncovalent dimers? A benchmark study using Gaussian09. *J. Comput. Chem.* **2013**, *34*, 1341-1353.

(60) Runge, E.; Gross, E. K. U. Density-Functional Theory for Time-Dependent Systems. *Phys. Rev. Lett.* **1984**, *52*, 997-1000.

(61) CASIDA, M. E. In *Recent Advances in Density Functional Methods*; WORLD SCIENTIFIC: 2011, p 155-192.

(62) Petersilka, M.; Gossmann, U. J.; Gross, E. K. U. Excitation Energies from Time-Dependent Density-Functional Theory. *Phys. Rev. Lett.* **1996**, *76*, 1212-1215.

(63) Burke, K.; Werschnik, J.; Gross, E. K. U. Time-dependent density functional theory: Past, present, and future. *J. Chem. Phys.* **2005**, *123*, 062206.

(64) Gadre, S. R.; Bapat, S. V.; Sundararajan, K.; Shrivastava, I. H. A GENERAL PARALLEL ALGORITHM FOR THE GENERATION OF MOLECULAR ELECTROSTATIC POTENTIAL MAPS. *Chem. Phys. Lett.* **1990**, *175*, 307-312.

(65) Gadre, S. R.; Kulkarni, S. A.; Shrivastava, I. H. MOLECULAR ELECTROSTATIC POTENTIALS - A TOPOGRAPHICAL STUDY. *J. Chem. Phys.* **1992**, *96*, 5253-5260.

(66) Wang, C.; Wang, J.; Wu, N.; Xu, M.; Yang, X.; Lu, Y.; Zang, L. Donor-acceptor single cocrystal of coronene and perylene diimide: molecular self-assembly and charge-transfer photoluminescence. *RSC Adv.* **2017**, *7*, 2382-2387.

(67) Hughes, J. M.; Hernandez, Y.; Aherne, D.; Doessel, L.; Müllen, K.; Moreton, B.; White, T. W.; Partridge, C.; Costantini, G.; Shmeliov, A.; Shannon, M.; Nicolosi, V.; Coleman, J. N. High Quality Dispersions of Hexabenzocoronene in Organic Solvents. *J. Am. Chem. Soc.* **2012**, *134*, 12168-12179.

(68) Lu, G.; Shi, G. Electrochemical polymerization of pyrene in the electrolyte of boron trifluoride diethyl etherate containing trifluoroacetic acid and polyethylene glycol oligomer. *J. Electroanal. Chem.* **2006**, *586*, 154-160.

(69) González-Piñuela, C.; Alonso-Salces, R. M.; Andrés, A.; Ortiz, I.; Viguri, J. R. Validated analytical strategy for the determination of polycyclic aromatic

compounds in marine sediments by liquid chromatography coupled with diode-array detection and mass spectrometry. *J. Chromatogr. A* **2006**, *1129*, 189-200.

(70) Mahmood, Z.; Zhao, J. Thiol-Activatable Triplet–Triplet Annihilation Upconversion with Maleimide-Perylene as the Caged Triplet Acceptor/Emitter. *J. Org. Chem.* **2016**, *81*, 587-594.

# TOC Graphics

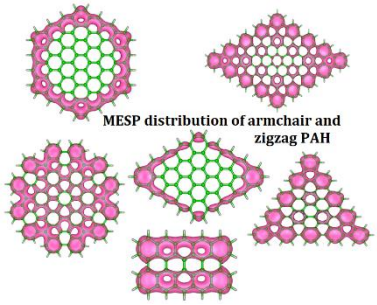


Polycyclic aromatic hydrocarbons (PAH) with various sizes and shapes in armchair and zigzag configurations have been analysed for their molecular electrostatic potential (MESP) features. The analysis provided an accurate description of the electron rich/deficient features of them, with respect to their sizes and shapes and found to be useful for the design and tuning of the optoelectronic properties of (PAH)donor-(π)spacer-(PAH)acceptor systems.